In situ x-ray diffraction topography studies on the phase formation in thin yttrium hydride

Remhof, A.; Song, G.; Sutter, Ch.; Labergerie, D.; Zabel, H.; Haertwig, J.

published in
Physical Review B. Condensed Matter and Materials Physics
2000

DOI (link to publisher)
10.1103/PhysRevB.62.2164

document version
Publisher's PDF, also known as Version of record

In situ x-ray diffraction topography studies on the phase formation in thin yttrium hydride films

A. Remhof, G. Song, C. Sutter, D. Labergerie, M. Hübener, and H. Zabel
Ruhr-Universität Bochum, Institut für Experimentalphysik/Festkörperphysik, D-44780 Bochum, Germany

J. Härtwig
European Synchrotron Radiation Facility, Boîte Postale 220, F-38043 Grenoble Cedex, France
(Received 7 February 2000)

Structural phase transitions in thin, epitaxial yttrium hydride films have been studied by means of synchrotron x-ray diffraction topography (XDT), complemented by atomic force microscopy and by measurements of the electrical resistance. Depending on the applied hydrogen pressure during the gas-phase loading experiments and the chosen temperature, different phases exhibiting different symmetries and electronic properties could be established. Despite the small scattering volume of the 200-nm-thick film, the phase nucleation, the spatial distribution of domains as well as the lateral hydrogen diffusion could be observed. Those experiments demonstrate the feasibility of XDT to study structural properties like the dynamics of phase transitions in thin epitaxially grown films on the nanometer scale. From the progression of the domain boundary between the YH_2 and YH_3 phase the hydrogen mobility was determined to 5×10^{-6} cm^2/s at 300 °C. Comparing high-temperature topographies with room-temperature results confirms that the phase boundary is narrower at high temperatures. Finally resistance measurements of Y/Nb double layers with varying hydrogen concentration confirm clearly that the YH_3 phase is insulating and that the resistance of the yttrium layer increases proportionally to the degree of YH_3 phase precipitation. The layer system acts as a hydrogen concentration-dependent potentiometer and could be used as a hydrogen sensor.

I. INTRODUCTION

Among different hydrogen-metal systems, rare-earth (RE) metals and their chemical relatives, scandium, yttrium, and lanthanum are of special interest because of their ability to absorb up to three hydrogen atoms per metal atom.[1] Yttrium, like most heavy RE metals at room temperature, has the hcp $P6_3mmc$ structure[2] with lattice constants $a=3.3648$ Å and $c=5.732$ Å. The phase diagram of the Y-H system consists of three principle phases depending on the hydrogen concentration. At low concentrations (α phase), hydrogen in yttrium can be described as a lattice gas where the hydrogen atoms are distributed on interstitial sites of the host lattice. Above a critical H/Y ratio of 0.2, the dihydride phase (β phase) starts to precipitate in the CaF_2 cubic structure $Fm3m$, in which all tetrahedral interstitial sites of the fcc metal lattice are filled with hydrogen. This structural transformation consists of an expansion of the metal lattice along the *c* axis by typically 5%, accompanied by a rearrangement of the stacking sequence. Hydrogen saturation of the trivalent yttrium is reached in the trihydride phase. Within this γ phase the metal atoms regain their hexagonal stacking sequence, while the closed-packed planes are even further pushed apart, resulting in a *c*-axis expansion of about 15%. Within both phase transitions the expansion of the basel plane is negligible.[3,4]

The β-γ transition in yttrium hydride films gained much attention due to the spectacular changes in the optical transmission and its potential technical applications.[5] While YH_2 is a shiny metal, YH_3 is a transparent insulator with a band gap of 1.8 eV. This discovery contradicted earlier self-consistent band-structure calculations. Wang and Chou[6,7] as well as Dekker *et al.*[8] concluded a semimetallic behavior for YH_3 with a band overlap of 1.5 eV. Subsequently different theoretical approaches have been established to explain the band gap in YH_3.[9–13] The reversibility of the YH_2-YH_3 phase transition fueled the hope of technical applications and motivated many experimental studies, particularly on thin films. The dynamics of the system, especially the hydrogen diffusion, has been visualized recently by optical transmission measurements[14,15] as well as by electromigration studies.[16,17] This paper discusses the macroscopic structure of thin epitaxially grown single-crystalline Y films and the effect of hydrogen on it. The focus lies on the question of domain size, domain formation, and domain mobility. X-ray diffraction methods will be used as an imaging tool for obtaining laterally resolved spatial information. Subsequently the results of the diffraction experiments will be related to atomic force microscope (AFM) measurements and to electrical resistance measurements. Because of the high anisotropy of the lattice expansion, effects due to the epitaxy between Y and the substrates are negligible and therefore the thin-film results should be representative for the bulk behavior.

II. SAMPLE PREPARATION

The samples were prepared via molecular-beam epitaxy (MBE) in a Riber EVA 32 MBE evaporation chamber. The Y (0001) films with a typical thickness of 200 nm were grown on Al_2O_3 $(11\bar{2}0)$/Nb (110) substrates and capped successively with Nb and Pd. The epitaxial relation between Al_2O_3 and Nb as well as between Nb and Y are well known and have been described in much detail. For Nb on Al_2O_3 the reader is referred to Refs. 18–21; for Y on Nb the reader is referred to Refs. 4 and 22. While the buffer guarantees

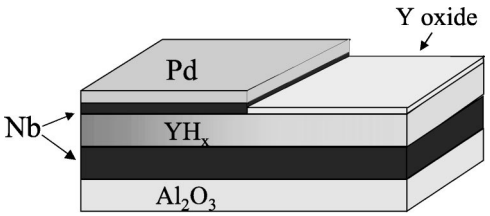

FIG. 1. Architecture of samples used in the x-ray diffraction topography experiments. One-half of the sample is Pd covered to allow the study of lateral hydrogen diffusion.

epitaxial growth, the Pd cap layer serves as a hydrogen window and as protection against corrosion. Details of the sample preparation may be found in Ref. 4. In order to study the different stages of hydrogenation, only one-half of the samples was covered with Nb and Pd. In ambient air, the uncovered part of the sample oxidizes on the surface. After the formation of an oxide layer of a typical thickness of several nm, the oxidation process stops. The body-centered-cubic oxide Y_2O_3 is known to be protective. Therefore the natural oxide layer of yttrium is often used to cover rare-earth films and superlattices.[23] The following hydrogenation experiments prove that Y_2O_3 is also an effective barrier for hydrogen. The sample architecture is displayed in Fig. 1.

III. EXPERIMENTAL METHOD

X-ray diffraction topography (XDT) is an imaging technique for single crystals based on Bragg diffraction. XDT exploits local variations of the sample reflecting power. Thus it visualizes inhomogenities such as defects, domains or phases within the crystal under investigation. Reviews on XDT may be found in Refs. 24 and 25. When using a zero-dimensional detector (counter) as employed in most diffraction methods, this information is averaged out and consequently lost. Those conventional experiments deliver detailed information about the crystalline structure of a given material on an atomic scale. They do not yield any spatially resolved information about the phase nucleation, the domain size, and the distribution of domains during phase coexistence or about the lateral hydrogen diffusion within a sample. All these questions may be investigated by XDT.

Figure 2 schematizes the main idea of the topographic methods. By using parallel and monochromatic radiation, a connection between a point *P* of the two-dimensional image on the position-sensitive detector (for example, a photographic film) and a small volume *V* within the sample is established. In a heteroepitaxial system all lattice planes are parallel but different films exhibit different lattice spacings. The same holds true for different hydride phases within a *c*-axis grown Y film. In this case, using monochromatic radiation, the reflections of the different materials occur at different incident angles. Rotating the sample about an axis normal to the scattering plane, the reflections of the different films (regions of different phases) will be spatially separated on the photographic film, as shown in Fig. 3. This *lattice parameter contrast* will be used later on to distinguish between the epilayers (Nb and Y) and the substrate and to visualize the development of the hydride phases within the Y film.

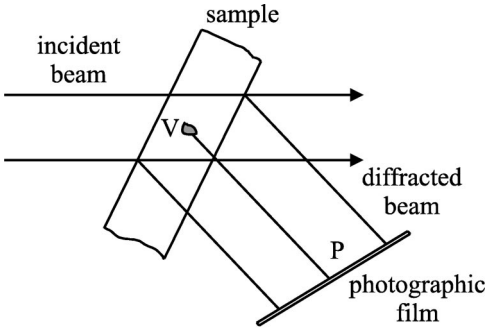

FIG. 2. Principle scattering geometry for x-ray diffraction topography.

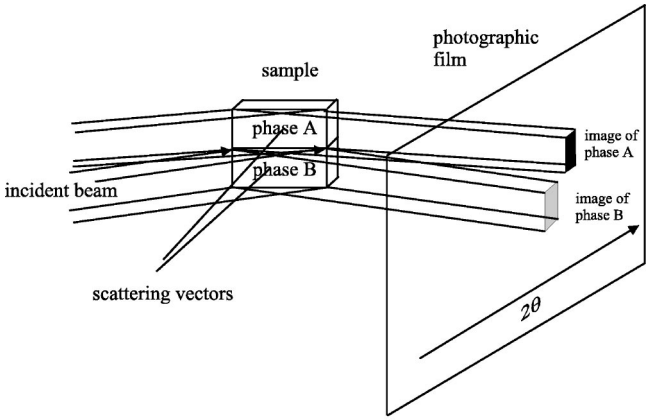

FIG. 3. X-ray scattering by a crystal consisting of two different and spatially separated phases A and B.

The XDT studies presented in this paper were performed at the imaging beamline ID19 at the European Synchrotron Radiation Facility (ESRF) in Grenoble, France. The characteristics of the beamline derive from the requirement of having a spatially extended, monochromatic beam, a high photon flux, and a tunable photon energy in the range of 8–120 eV. The small divergence of the beam (0.3×0.1 mrad^2) leads to the choice of a 140-m-long beamline. Within this distance from the source, a high-magnetic-field wiggler with a variable gap, a homogeneous beam of 40×14 mm^2 allows us to illuminate extended samples. The source guarantees a high photon flux at the sample position, minimizing exposure times. A HASYLAB-style double-crystal, fixed-exit monochromator allows us to select a monochromatic beam out of the wiggler spectrum. A photon energy of 14 keV, close to the Mo K_α line, was chosen. Further details of the beamline characteristics can be found in the beamline handbook of the ESRF. The height of the beam was limited to 7 mm by the windows of the vacuum chamber. The 10×20 mm^2 big sample was mounted horizontally, i.e., with the long side perpendicular to the scattering plane. Due to the large horizontal width of the beam, covering the whole width of the sample, an area of 10×7 mm^2 of the sample was illuminated. The angle of incidence of the parallel and monochromatic beam could be varied by rotating the sample about an axis perpendicular to the incident beam. A photographic film was employed as an open detector, covering a wide angular range. The *Kodak Professional Industrex SR* used for this experiment allows us to record all specular Bragg reflections of the sample within one exposure. The exposure times were

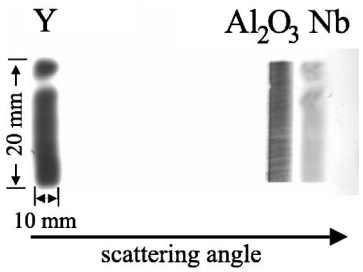

FIG. 4. Topographic image of the virgin sample as shown in Fig. 1. From left to right the reflections of the yttrium layer, the sapphire substrate and the niobium buffer are displayed. During the x-ray exposure time, the incident angle was continuously changed by rocking the sample. The gaps in the Y and Nb exposures are due to shadowing by the wire used during the growth of the sample.

adjusted according to the scattering volume of the constituencies of the sample. For the sapphire substrate an exposure time of 1 s was chosen; the reflections of the epilayers were recorded in about 100 s. Different lattice parameters of the different metals evaporated onto the substrate allow us to separate their images spatially on the photographic film by their different Bragg angles. The topographic images were recorded in two different ways. First, in order to visualize the orientations of the structural domains within the sample, images were taken at several fixed positions on the rocking curve. Second, the sample was rocked during the exposure to collect all the reflected intensities from the differently oriented domains. Due to the high collimation of the incident beam the spatial resolution of the XDT method is only limited by the grain size of the photographic film, which is about 1 μm.

IV. RESULTS AND DISCUSSION

A. The virgin sample

Figure 4 is a typical topographic image of the virgin sample. From left to right, corresponding to an increase of the scattering angle, the reflections of the yttrium layer, the sapphire substrate, and the niobium layer can be seen. The trace of the wire used to fix the substrate during the growth process can clearly be observed on the recorded images of the two metallic layers. As in Fig. 4 all samples were mounted such that the wire is horizontal and in the upper part of the sample. For the interpretation of the images it is important to realize that the topographies are horizontally compressed. Taking into account the sine of the Bragg angle, the compression factor in our case is about 10.

The topographic images of the metal layers exhibit many details. Images taken at different fixed incident angles illustrate which domains contribute to the reflected intensity at a specific point of the rocking curve. Figure 5 displays two topographic images of the niobium buffer layer recorded on the wing (image A) and at the center of the rocking curve (image B), respectively. At first glance both images appear almost uniform, indicating a homogeneous film. An optical microscope was employed to obtain more details from the exposed and developed photographic film. An enlarged section of Fig. 5A is shown in Fig. 6. Single mosaic blocks become visible. Their shapes are well defined by sharp borders and an abrupt change of contrast to the background. The size of these mosaic blocks is estimated to be on the order of 10 μm.

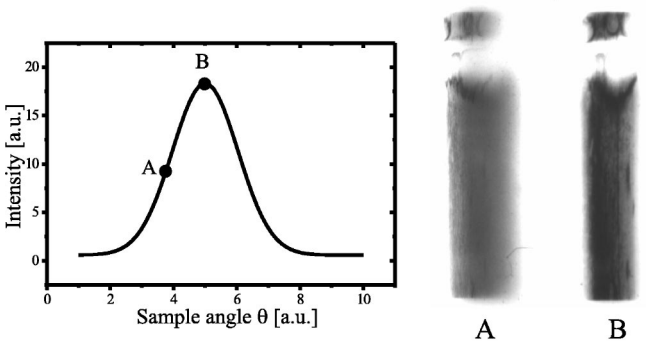

FIG. 5. Topographic images of the Nb buffer layer prior to hydrogen loading. The images were recorded at different incident angles, corresponding to positions on the wing of the rocking curve (A) and on the center of the rocking curve (B).

The sharp contrast between the blocks indicates that each block has its own orientation, independent and uncorrelated from its surrounding. Such a mosaic block does not necessarily represent a perfect single crystal. As known from grazing incidence x-ray diffraction experiments,[4] the in-plane coherence length is much smaller than the topographically detected size. Also measurements carried out by transmission electron microscopy show a dislocation density, which require defect-free domain sizes on the order of about 20 nm. Thus a mosaic block has to be considered to be composed of several single-crystalline domains of the same orientation, separated by dislocation lines.

The yttrium layer has a different appearance. Unlike the Nb layer, the Y film appears to be more coherent. The topographic images show smooth changes of contrast, suggesting a continuous distribution of crystal orientations. As expected by the independent in-plane expansions of the Nb and Y layers,[4] there is no influence of the Nb buffer on the microstructure of the Y film. While the Nb layer shows well-defined structures in the μm range, the Y film exhibits much larger features in the mm range. The two topographic images displayed in Fig. 7 demonstrate nicely the ''negative image effect'': those volume elements that fulfill the Bragg condition at the center of the rocking curve (images B and B′) do not contribute to the intensity in the flanks of it (images A and A′). As a result, one topography appears to be the negative image of the other one.

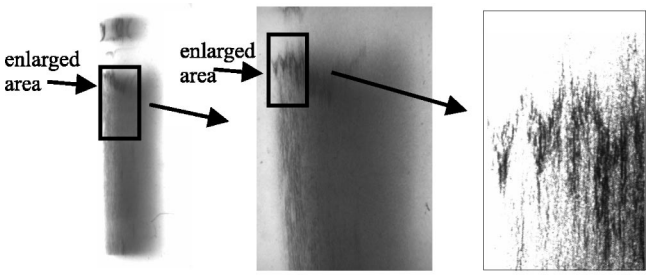

FIG. 6. Enlarged portion of the topographic image from the Nb buffer layer obtained by an optic microscope.

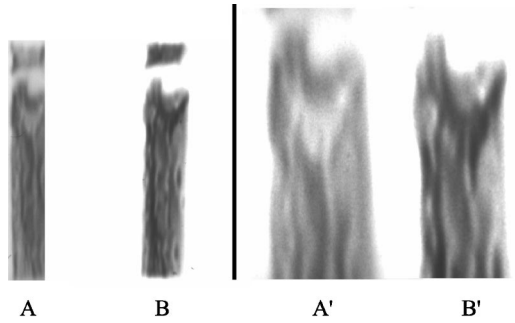

FIG. 7. Topographic images of the Y layer prior to hydrogen loading. The images were recorded at different incident angles, corresponding to positions on the wing (A) and at the center of the rocking curve (B). A' and B' are enlarged areas of A and B, respectively.

B. Hydrogen loading and phase formation

Exposing the sample to hydrogen atmosphere leads to fast hydrogen loading of the yttrium and of the niobium layers beneath the palladium-covered part. Thermodynamic equilibrium with the surrounding atmosphere is achieved within several minutes. Afterwards lateral hydrogen diffusion starts, accompanied by the structural phase transitions as described in Sec. I. A series of topographic images at increasing pressures is displayed in Fig. 8, showing the hydrogenation of the initially virgin sample. All images were taken at 300 °C. Each one depicts a 7-mm-long part of the sample, limited by the trace of the wire. Due to the geometrical effects mentioned before, the image of the 10-mm-wide sample is compressed to about 1 mm on the photographic film. In order to record all domains of a given phase irrespective of their orientations, the sample was rotated during the exposure about the axis normal to the diffraction plane. Therefore structural details are averaged out and each particular phase appears

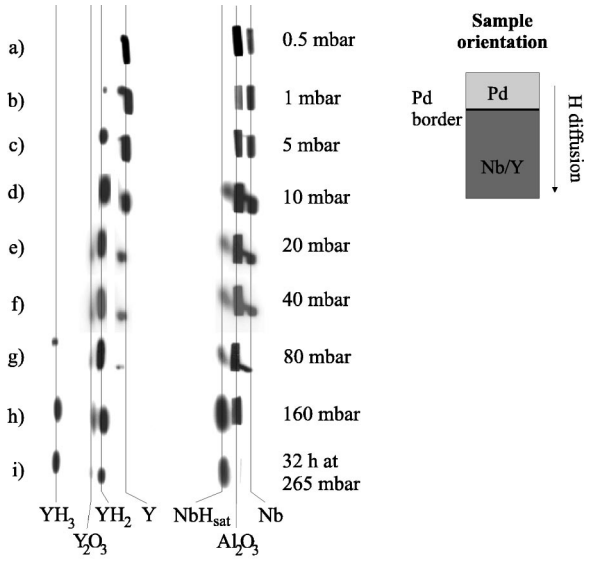

FIG. 8. Series of x-ray diffraction topographies of the first hydrogenation of the sample shown in Fig. 1. The series of images (a)–(i) is taken at $T=300$ °C and at the respective hydrogen pressures. The inset explains the sample orientation used. The vertical lines are guides to the eye for the positions of the different Bragg reflections.

uniformly gray. At hydrogen pressures below 1 mbar, hydrogen dissolves in the palladium-covered part of the yttrium layer, forming a lattice gas. The expansion of the lattice causes a decrease of the scattering angle. Therefore the yttrium reflection shifts to the left-hand side in the upper part of the image representing the yttrium layer. The precipitation of YH_2 starts at about 1 mbar, occurring simultaneously at arbitrary places in the Pd-covered part of the sample. This process may be compared with the wetting of the floor after it starts raining. Between the two extreme states ''dry'' (α phase) and ''wet'' (β phase) both ''phases'' coexist lateraly. There is no spatial separation or segregation of the phases. The homogeneously distributed YH_2 domains must be smaller than 1 μm (film resolution). The Bragg peaks for the α and β phase are well separated in angular space, indicating again that the transition between these two phases is discontinuous. Up to 1 mbar, there is no detectable expansion effect of the Nb buffer layer; all hydrogen is absorbed by the yttrium.

At a pressure of 5 mbar, the transition to the β phase is completed below the Pd-covered part of the sample. Also the Nb buffer beneath the YH_2 is saturated with hydrogen. Unlike the Y, Nb does not cross a phase boundary between the hydrogen-free state and the saturated state as the experiments were carried out well above the critical temperature for Nb-H which is at 170 °C. There is a continuous shift of the lattice parameter along the hydrogen concentration gradient within the sample. As a result, the topographic images of the hydrogen-free part of the Nb film and of the hydrogen-loaded part are not isolated as in the case of Y. They are connected, indicating that the gradient in the lattice parameter is caused by a gradient of the hydrogen concentration.

A further increase of the hydrogen pressure initiates the lateral diffusion of hydrogen from top to bottom, both in the Y film as well as in the Nb buffer layer. There is no sharp diffusion front visible in the Y film. A region of coexisting α and β phases can still be observed. Similar to the situation at 1 mbar, their domains are smaller than the film resolution and both phases are completely mixed.

Thermodynamically the diffusion front has to be a continuous line in a homogeneous medium. Therefore the occurrence of a large region of phase coexistence in a diffusion experiment seems to contradict the laws of thermodynamic. However, in the present case the medium is not homogeneous and domains of both phases coexist. Obviously the hydrogen finds diffusion paths in the film where it can advance faster in one region than in others, leaving domains of lower hydrogen concentration behind.

The γ phase starts to nucleate at a pressure of 80 mbar. Like the occurrence of the β phase at 1 mbar, both phases coexist beneath the Pd cap layer before the hydrogen-rich phase starts to diffuse along the sample at higher pressures. During the diffusion process, the phase border of the YH_3 behaves similar to the YH_2 border. There is no visible change in the domain size. Again a region of phase coexistence propagates in front of the homogeneous YH_3 phase. Hydrogen diffusion within the investigated sample is slow, especially in the YH_3 phase. Even after 36 h in a hydrogen atmosphere of 265 mbar the hydrogen front line of the YH_3 phase just moved 2 mm while the rest of the Y film changed completely to YH_2. At this stage of the experiment the Nb

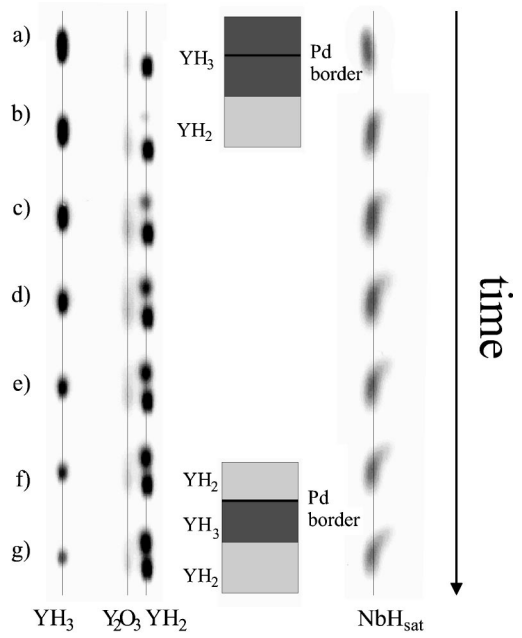

FIG. 9. Series of XDT images during dehydrogenation at 300 °C. First, the Pd-covered part switches to the YH_2 phase, than the hydrogen within the remaining YH_3 phase diffuses towards the Pd limit, where it escapes from the sample. This process is illustrated by the two sketches representing the phase distribution within the sample in the first and the last images.

buffer layer is saturated with hydrogen. Surprisingly, there is no hydrogen diffusing from the Nb buffer to the YH_x film. In other words, the NbH_x film is not short circuiting the lateral hydrogen pathway in the YH_x film. Due to the low velocity of the diffusion, thermodynamic equilibrium has not been achieved in any of the topographic images in Fig. 8.

An investigation of the YH_3, the YH_2, and the Nb reflections at different points of their respective rocking curves does not provide any special features. The topographic images appear to be uniformly gray. Hydrogen loading destroys all the structural features that were visible in the virgin state of the sample and averages out all details of the domain structures.

Removing the hydrogen atmosphere completely and keeping the temperature constant at 300 °C expels the hydrogen partially from the sample as shown in Fig. 9. The exposure times were kept constant at 300 s for the YH_3 and the YH_2 reflections together and at 500 s for the Nb reflection, summing up to a total of 800 s for one complete exposure. Immediately after finishing one exposure, the next one was started. The first topographic image in Fig. 9 is identical to the last one in Fig. 8. Between the first and the second one, the hydrogen was pumped out of the chamber.

Desorption of the hydrogen takes place through the Pd cap layer. First the hydrogen becomes expelled from the Pd-covered part. On the third and fourth exposure a coexistence of YH_3 and YH_2 can clearly be seen. As a result, the yttrium underneath the Pd cap layer as well as in the bottom part of the sample exists in the β phase, separated by a middle part, predominantly occupied by the γ phase. Later on the hydrogen from this middle region diffuses towards the Pd window, where it escapes from the sample, causing the γ phase to vanish gradually. The Nb reflection behaves differently as the lattice parameter is allowed to change continuously within a hydrogen gradient. On the first topographic image exposed under hydrogen atmosphere, the Nb reflection is inclined, demonstrating a lattice parameter gradient. Under the Pd-covered part the lattice parameter is higher than at the bottom of the sample. Immediately after removing the hydrogen atmosphere, the hydrogen starts leaving the Nb layer via the Pd window. Now the hydrogen concentration and the lattice parameter rise toward the bottom of the sample. As time passes on and more hydrogen gets expelled, the Nb reflection moves back towards its initial position without completely reaching it during this experiment.

C. Lateral phase propagation

Exposing a partially Pd-covered Y layer to a hydrogen atmosphere leads to the fast formation of the YH_3 phase underneath the Pd cap layer while the rest of the Y layer is still hydrogen free. The resulting steep hydrogen concentration gradient in the Y layer close to the Pd border is the driving force behind the lateral phase propagation in the sample. Due to the large miscibility gaps in the H-Y system the hydrogen concentration cannot vary continuously within the sample. The lateral hydrogen progression therefore requires two mechanisms. First, the hydrogen atoms have to diffuse from the Pd-covered part to the phase boundary. Then new domains of the hydrogen-rich phase have to nucleate. The phase boundary moves through the sample by the continuous precipitation of new domains. This heterogeneous seed formation consumes energy that is nessesary to plastically deform the crystal lattice and to build up domain walls. During the α-β transition as well as during the β-γ transition, the heterogeneous seed formation is the process that limits the velocity of the phase propagation.

Generally, the net flux **J** of impurity atoms is related to the gradient of the impurity concentration c by a phenomenological relation called Fick's first law:

$$\mathbf{J} = -D\,\mathrm{grad}(c), \tag{1}$$

where D is the diffusion constant related to the mobility of the impurity atoms. D may explicitly be concentration dependent, symbolized by $D(c)$. Particle conservation requires $\partial c/\partial t = -\mathrm{div}\mathbf{J}$, leading to Fick's second law:

$$\frac{\partial c}{\partial t} = \mathrm{div}[D(c)\,\mathrm{grad}(c)]. \tag{2}$$

In the present diffusion situation, only one spatial dimension has to be considered. Fick's second law then takes the form

$$\frac{\partial c}{\partial t} = \frac{\partial}{\partial z}\left(D(c)\frac{\partial c}{\partial z}\right), \tag{3}$$

where z is the lateral distance in the sample plane. Boltzmann showed that Fick's second law can be transformed into a relation of only one variable $\lambda = z/\sqrt{t}$, if the boundary conditions can be transformed accordingly.[26] This transformation still holds in multiphase systems[27,28]

$$\lambda\frac{dc}{d\lambda} = -2\frac{d}{d\lambda}\left(D(c)\frac{dc}{d\lambda}\right). \tag{4}$$

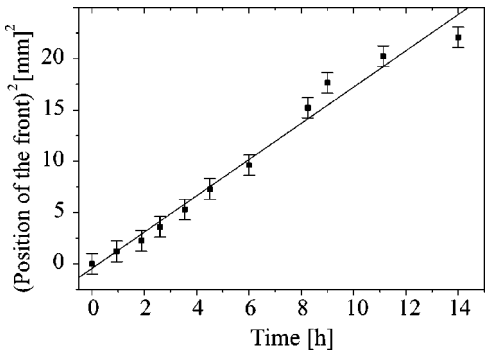

FIG. 10. The square of the position of the YH_3 phase boundary as a function of time at $T=300\,°C$ in a hydrogen atmosphere of 800 mbar. The solid line is a linear fit to the data points.

The validity of this Boltzmann scaling in the Y-H system has been demonstrated by den Broeder and co-workers[14] on a 3000-Å-thick Y layer by optical transmission measurements.

To deduce the diffusion coefficient $D(c)$, the concentration as a function of λ, $c(\lambda)$ has to be known. Those data could be obtained mapping the concentration by nuclear profiling methods or, in the case of H in Y, by optical methods. However, the effective mobility of the phase boundary $M_{eff}=z^2/t$, where z denotes the position of the diffusion front of the phase boundary can directly be measured. den Broder *et al.* investigated the temperature dependence of M_{eff} and obtained an Arrhenius behavior between room temperature and 140 °C and at a hydrogen pressure of 1000 mbar. M_{eff} can then be expressed as $M_{eff}=M_0 \exp(-E_a/kT)$. The activation energy and the M_0 were determined to be 0.369 eV and 1.4×10^{-3} cm^2/s, respectively.

As the motion of the phase boundary can clearly be seen, M_{eff} is also easily accessible in XDT measurements. To obtain a value for the mobility of the YH_3-YH_2 phase boundary, a second loading experiment was carried out at a constant temperature of 300 °C and a constant hydrogen pressure of 800 mbar. The progression of the YH_3 front as a function of time is represented in Fig. 10. Due to the rather large YH_2-YH_3 coexistence area, the position of the diffusion front has to be defined in the same way for all topographic images. For the calculation of the phase mobility the front of the coexistence region has been chosen. The error bars in Fig. 10 originate from the uncertainty of determining this border line.

The progression of the YH_3 diffusion front follows a $\sqrt{t}$ law, indicating the validity of the Boltzman scaling. A fit to the data points reveals an effective mobility of $M_{eff}=5\times10^{-6}$ cm^2/s. Extrapolating the results of den Broeder *et al.* [14] to 300 °C results in an effective mobility of 8.2×10^{-7} cm^2/s, which is about one order of magnitude slower than in the present experiment. Unfortunately a single value of the effective mobility measured at one specific temperature and one specific hydrogen pressure does not allow determining the activation energy. Thus additional experiments are necessary to determine the kinetics of hydrogen in epitaxial Y films.

D. The narrowing of the miscibility gap at elevated temperatures

After 20 h at 300 °C in a hydrogen atmosphere of 800 mbar, the lower half of the Y film still shows no trace of the γ phase. It completely remains in the β phase. On the other hand, after cooling the sample to room temperature, the topographic image of the lower part of the sample clearly shows the appearance of YH_3 (Fig. 11). The sudden nucleation of the γ phase can be explained by the Y-H phase diagram.[1] At elevated temperatures the miscibility gap between the β and the γ phase becomes more narrow. In other words, the hydrogen concentration of the saturated β phase increases with temperature. Vice versa, as the temperature is lowered, the surplus of the hydrogen precipitates into the hydrogen rich γ phase.

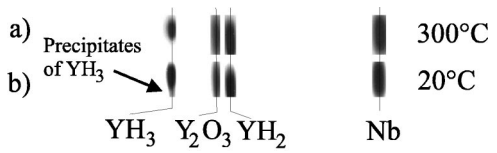

FIG. 11. X-ray diffraction topography comparison of the saturated β phase at 300 °C and at room temperature, showing the precipitation of the γ phase.

V. OPTICAL APPEARANCE AND AFM STUDIES OF A PARTIALLY LOADED SAMPLE

The different diffusion fronts as well as the coexistence regions can be identified by the optical appearance of the sample. In Fig. 12 an optical photograph of the sample is shown in a state corresponding to the lower part of Fig. 11. The image was recorded using an optical microscope in reflection mode and a black and white video camera. The sample itself was illuminated from the top with white light. The upper third of the sample is covered with Pd. The trace of the wire as well as the sharp change of contrast at the Pd border are clearly visible. The YH_3 diffusion front coincides with another change in the reflected intensity about 8 mm away from the trace of the wire. Comparing the different gray scales, the region of phase coexistence can be distinguished from the homogeneous phases, as marked in Fig. 12. Within the lower part of the sample parallel stripes of up to 4 mm length and of 0.1 mm width are visible. Those stripes may be attributed to the precipitates of YH_3 which have been discussed in the previous paragraph. Their shape, their incli-

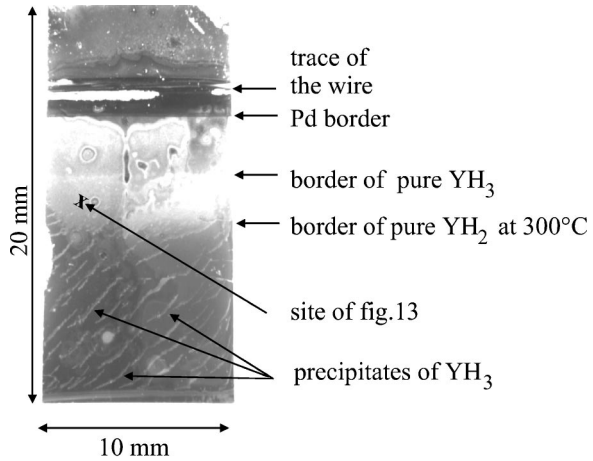

FIG. 12. Optical photography of the partially hydrogen-loaded sample as used in the second exposure of Fig. 11.

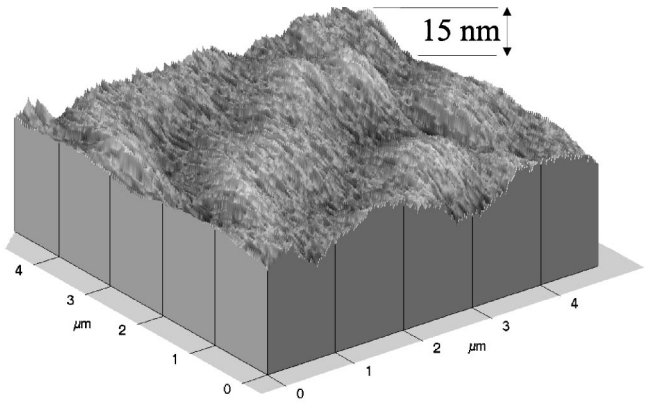

FIG. 13. AFM image of the partially hydrogen-loaded sample. The displayed surface profile was measured in the YH_2-YH_3 phase coexistence region of the sample (compare Fig. 12).

nation with respect to the sample edges, as well as their parallelity are presently not understood.

Apart from the basic features described above, the sample exhibits many more details like cloudy stains or streaks. Without further studies, explanations of those details are the subject of speculation. They may be due to hydrogen density fluctuations, to chemical impurities, or to yttrium oxides.

Although a thin oxide layer covers the sample, the surface topology of the partially hydrogenated sample still reflects the different stages of hydrogenation. As the out-of-plane lattice parameter of YH_2 and YH_3 differs by 10%, the overall thickness of the sample varies as well. Since the thickness of the Y film is 200 nm, in the region of phase coexistence the thickness variations should be on the order of about 20 nm.

Since the expected domain size is on the order of 1 μm, an atomic force microscope (AFM) is the ideal tool for recording the surface profile of the sample. Figure 13 shows a 5×5 μm^2 area of the sample within the region of phase coexistence. The surface reminds us of a hilly landscape with gentle slopes. Typical sizes of the hills match the expected domain proportions. The height difference between the lowest and the highest point of the displayed area equals 15 nm. This is five times more than the original height fluctuations from the surface roughness of the oxide layer. AFM images taken in single-phase regions show an average roughness of about 2–3 nm. While the lateral extension of the surface structures as well as their heights correspond to the expected values, their shape does not. Assuming columns of YH_2 and of YH_3 with their respective film thickness, a surface topology with sharp contours would have been expected. The YH_3-YH_2 borderline should result in a steep surface step, separating flatter areas. But it is important to recall that with AFM the actual surface of the sample is scanned, which in this case is covered by Y_2O_3. The oxide layer may smoothen the discontinuities between the different phases.

VI. ELECTRICAL RESISTANCE MEASUREMENTS

Measuring the electrical resistance together with the diffracted x-ray intensity during *in situ* loading of the sample with hydrogen offers the opportunity to monitor simultaneously the structural aspects of the phase transition and the electronic aspects.

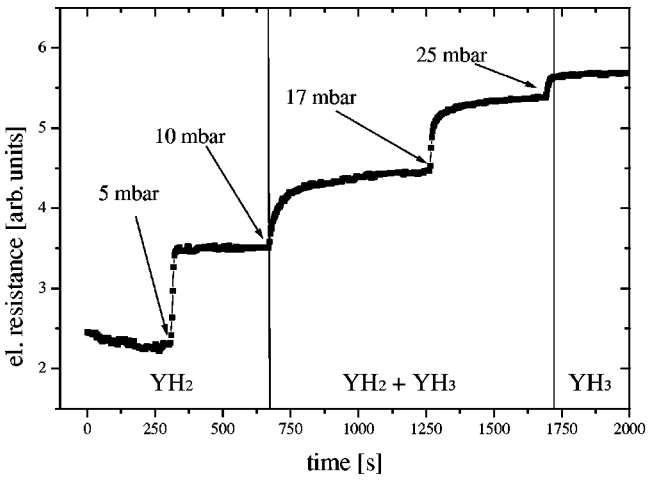

FIG. 14. Electrical resistance of a Y/Nb sample as a function of time and for different hydrogen pressures. Starting from YH_2, the hydrogen pressure was successively increased up to the YH_3 phase. The resistance step at 300 s after increasing the H pressure from 5 to 10 mbar result from saturation of the Nb buffer layer with hydrogen. Subsequent changes of the resistance are due to the gradual phase transition from YH_2 to YH_3.

Within this experiment a different sample design was used. The Y layer was completely covered with a Nb/Pd cap to exclude lateral diffusion. The electrical resistance was measured by an usual four-probe method. The current in-plane (cpp) geometry averages the resistance of the whole sample. Since the sample contains a niobium buffer layer as well as a palladium cap layer, the change of the electrical resistance due to hydrogen loading is affected by the response of all layers in the sample. Fortunately the energy gain per hydrogen atom dissolved into the lattice is smaller in YH_2 than in Nb. Therefore the transition from YH_2 to YH_3 starts only after the niobium layers are saturated with hydrogen. The XDT experiments clearly show in Fig. 8 that the yttrium layer remains in the β phase as long as the niobium buffer is not saturated with hydrogen.

All resistance measurements presented in this paper were performed at 200 °C. This temperature was chosen because the hydrogen solubility and resistance of Nb films have been extensively studied at this temperature, allowing us to separate the resistance changes of both materials.[29] In order to distinguish between the different metal layers, the starting condition was prepared such that the Y layer was in the YH_2 phase while the niobium was almost hydrogen free.

Figure 14 shows the development of the electrical resistance as a function of time. At a time $t=300$ s, 5 mbar of H_2 gas were introduced into the chamber. The Nb buffer is immediately saturated with hydrogen, while the Y is still in the YH_2 phase. The sudden increase of the electrical resistance is entirely due to hydrogen in the Nb film. Both the time scale as well as the absolute change of resistance are the same as for a single Nb layer of the same thickness under the same conditions.[29] Subsequently the hydrogen pressure was increased step by step up to a pressure of 25 mbar. All additional resistance changes originate from the Y layer. Each time the electrical resistance reached equilibrium, a radial x-ray scan was performed. These scans show that the increase of the electrical resistance is accompanied by a suc-

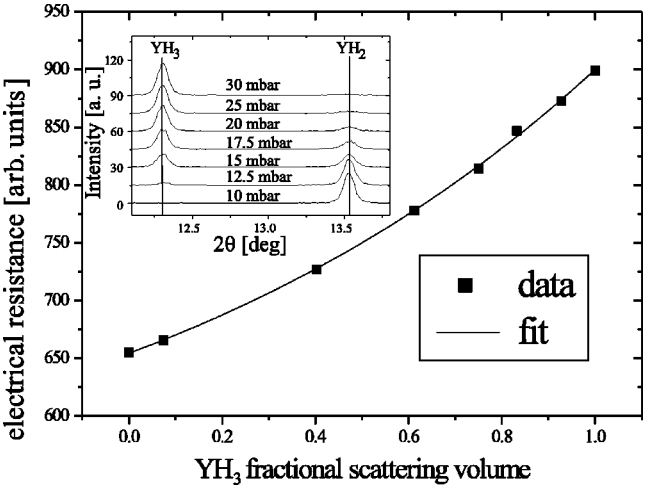

FIG. 15. Plot of the electrical resistance versus the fractional scattering volume. The inset shows the corresponding radial x-ray scans covering the YH_2 and YH_3 phase.

cessive structural phase transition from YH_2 to YH_3 as shown in the inset of Fig. 15. In Fig. 15 is plotted the fractional scattering volume of YH_3, i.e., the integrated (0002) Bragg intensity, versus the resistance. The increase of the resistance can be described by a model of two parallel resistors. The YH_x layer is represented by a tunable resistor while the resistance of the Nb buffer is assumed to be constant. In a system of parallel resistors it is more convenient to use conductivities rather than resistivities. Assuming an electrical conductivity close to zero for the pure YH_3 state, the conductivity of the whole system may be written as

$$\sigma_{total} = \sigma_{Nb} + (1-x)\sigma_{YH_2}, \tag{5}$$

where x is the fractional volume of YH_3 as determined by x-ray scattering. The conductivity of the buffer, σ_{Nb}, and of the YH_2 film, σ_{YH_2}, can be deduced from the final conductivity ($x=1$) and from the initial conductivity ($x=0$), respectively. The solid line in Fig. 15 is a fit to the data points using this simple model. In spite of its simplicity the quality of the fit is striking. Several conclusions can be drawn. First, YH_3 is indeed a bad conductor or an insulator in agreement with the literature. Second, this experiment proves that during the phase coexistence the Y film is composed of two structurally distinct phases possessing distinct electrical resistivities. In other words, the YH_x can be visualized as a 2D arrangement of YH_2 and YH_3 crystallites. A change of the resistance is only possible together with a change of the fractional volumes of the participating phases. The Nb buffer layer provides pathways for electrons around YH_3 blockages in the YH_x film near the YH_x/NbH_x interface at high-x values. Thus the Nb buffer allows us to measure σ_{YH_2} for $0 \leqslant x \leqslant 1$. Otherwise the conductivity measurement would be limited to the percolation threshold.

VII. CONCLUSION

On a macroscopic scale, thin epitaxial layers of Nb and Y grown on sapphire substrates appear quite differently. Nb shows distinct mosaic blocks of several μm in diameter, indicating an incoherent composition of the crystalline layer. Y, on the other hand, shows larger structures with smoothly varying orientation, suggesting a more coherent structure. No correlation between the structural details of the buffer layer and the Y layer could be detected. Exposing a Pd covered Y film to a hydrogen atmosphere of a few mbar, domains of YH_2 nucleate at random places. With increasing hydrogen pressure the number of YH_2 domains increase until the whole film has changed to the β phase. At higher pressures, the formation of the YH_3 phase starts in the same way. Typical sizes of the domains are on the order of 1 μm. Within the hydride phases, the topographic pictures show no further details. The structural features of the virgin sample are averaged out.

Atomic force microscope images show enhanced thickness fluctuations in regions of the YH_2-YH_3 phase coexistence. Those originate from the different lattice spacings of the distinct phases, leading to different layer thicknesses. However, no sharp contours between YH_2 and YH_3 could be detected.

Hydrogen diffusion can be observed by the lateral progression of the phase boundary. At $p_{H_2}=800$ mbar and at 300 °C, the YH_3 front moves with an effective mobility of 5×10^{-6} cm^2/s.

In situ measurements of the electrical resistance together with the x-ray diffraction curves upon hydrogen loading allows us to relate the metal-insulator transition to the structural information. Starting with a pure YH_2 film, the electrical resistance increases with the amount of the nucleated hydrogen rich γ phase. The sample may be regarded as a hydrogen tunable potentiometer.

ACKNOWLEDGMENTS

We would like to thank R. Griessen, S. J. van der Molen, and B. Hjörvarsson for fruitful discussions. This work was supported by the Bundesministerium für Bildung und Forschung under Contract Nos. ZA4BC1 and ZA4BC2 and the EU-TMR project Metal-hydride films with switchable physical properties (Project No. ERB FMRX-CT98-187), which we gratefully acknowledge.

[1] P. Vadja, in *Handbook on the Physics and Chemistry of Rare Earth*, edited by K. A. Gschneidner and L. Eyring (Elsevier, Amsterdam, 1995), Vol. 20.

[2] R. W. G. Wyckoff, *Crystal Structures* (Interscience, New York, 1966), Vol. 1.

[3] T. J. Udovic, Q. Huang, and J. J. Rush, J. Phys. Chem. Solids **57**, 423 (1996).

[4] A. Remhof, G. Song, Ch. Sutter, A. Schreyer, R. Siebrecht, H. Zabel, F. Güthoff, and J. Windgasse, Phys. Rev. B **59**, 6689 (1999).

[5] J. N. Huiberts, R. Griessen, J. H. Rector, R. J. Wijngarten, J. P. Dekker, D. G. de Groot, and N. J. Koeman, Nature (London) **380**, 231 (1996).

[6] Y. Wang and M. Y. Chou, Phys. Rev. B **51**, 7500 (1995).

[7] Y. Wang and M. Y. Chou, Phys. Rev. Lett. **71**, 1226 (1993).
[8] J. P. Dekker, J. van Ek, A. Lodder, and J. N. Huiberts, J. Phys.: Condens. Matter **5**, 4805 (1993).
[9] P. J. Kelly, J. P. Dekker, and R. Stumpf, Phys. Rev. Lett. **78**, 1315 (1997).
[10] K. K. Ng, F. C. Zhang, V. I. Anisimov, and T. M. Rice, Phys. Rev. Lett. **78**, 1311 (1997).
[11] K. K. Ng, F. C. Zhang, V. I. Anisimov, and T. M. Rice, Phys. Rev. B **59**, 5398 (1999).
[12] R. Ahuja, B. Johansson, T. M. Wills, and O. Eriksson, Appl. Phys. Lett. **71**, 3498 (1997).
[13] X. W. Wangand and C. Chen, Phys. Rev. B **56**, R7049 (1997).
[14] F. J. A. den Broeder, S. J. van der Molen, M. Kremers, J. N. Huiberts, D. G. Nagengast, A. T. M. van Gogh, W. S. Huisman, N. J. Koeman, B. Dam, J. H. Rector, S. Plota, M. Haaksma, R. M. N. Hanzen, R. M. Jungblut, P. A. Duine, and R. Griessen, Nature (London) **394**, 656 (1998).
[15] M. Kremers, N. J. Koeman, R. Griessen, P. H. L. Notten, R. Tolboom, P. J. Kelly, and P. A. Duine, Phys. Rev. B **57**, 4943 (1998).
[16] R. Griessen, J. N. Huiberts, M. Kremers, A. T. M. van Gogh, N. J. Koeman, J. P. Dekker, and P. H. L. Notten, J. Alloys Compd. **253-254**, 44 (1997).
[17] E. S. Kooij, A. T. M. van Gogh, and R. Griessen, J. Electrochem. Soc. **146**, 2990 (1999).
[18] A. Remhof, G. Song, K. Theiss-Bröhl, and H. Zabel, Phys. Rev. B **56**, R2897 (1997).
[19] J. Mayer, C. P. Flynn, and M. Rühle, Ultramicroscopy **33**, 51 (1990).
[20] P. Sonntag, W. Donner, N. Metoki, and H. Zabel, Phys. Rev. B **49**, 2869 (1994).
[21] G. Gutekunst, J. Mayer, and M. Rühle, Philos. Mag. A **75**, 1329 (1997); **69**, 2510 (1995).
[22] J. Kwo, M. Hong, and S. Nakahara. Appl. Phys. Lett. **49**, 319 (1986).
[23] C. F. Majkrzak, J. Kwo, M. Hong, Y. Yafet, D. Gibbs, C. L. Chien, and J. Bohr, Adv. Phys. **40**, 99-189 (1991).
[24] *Diffraction and Imaging Techniques in Material Science*, edited by S. Amelinckx, R. Gevers, and J. van Landuyt (North-Holland, Amsterdam, 1978).
[25] J. Baruchel, in *Neutron and Synchrotron Radiation for Condensed Matter Studies*, edited by J. Baruchel, J. L. Hodeau, M. S. Lehmann, J. R. Regnard, and C. Schlenker (Springer-Verlag, Berlin, 1993).
[26] L. Bolzmann, Annalen der Physik **53**, 959 (1894).
[27] J. Crank, *The Mathemetics of Diffusion* (Clarendon, Oxford, 1975).
[28] Y. Adda and J. Philibert, *La Diffusion dans les Solides* (Inst. Nat. des Sciences et Techniques Nucléaires, Saclay, 1966).
[29] G. Song (private communication).